

Linker-Molecule-Free Gold Nanorod Films: Effect of Nanorod Size on Surface Enhanced Raman Scattering

Sukang Yun,^{†,||} Min Kyung Oh,[†] Seong Kyu Kim,^{*,†} and Sungho Park^{*,†,‡,§}

Department of Chemistry, Department of Energy Science, SKKU Advanced Institute of Nanotechnology, Sungkyunkwan University Suwon 440-746, South Korea, and New Business Development Team, R&D Business Laboratories, Hyosung Corporation, Kyonggi 431-080, South Korea

Received: March 19, 2009; Revised Manuscript Received: June 17, 2009

A methodology for synthesizing different sized gold nanorods and ordering them into a two-dimensional array at a water/hexane interface without a linker-molecule is reported. The resulting nanorod film was transferred to a solid substrate repeatedly, allowing for systematic control of the nanorod film thickness. An investigation into the thickness-dependent surface enhanced Raman scattering (SERS) of adsorbed molecules revealed different SERS enhancement as a function of the size of gold nanorods under similar experimental conditions. The SERS enhancement factor per layer of each nanorod size was obtained from a plot of the peak intensity versus the number of layers. The comparison of such values enables a systematic evaluation of the SERS enhancement of the resulting nanorod films. Theoretical consideration by discrete dipole approximation calculation and finite different time domain method was also performed and the local surface plasmon coupling was believed to induce such differences in the SERS enhancement.

Introduction

Anisotropic metal nanoparticles have received considerable attention in recent years because of their unique optical, electronic, and catalytic properties. Among the various nanostructures, the synthesis of gold and silver metal nanoparticles has been extensively developed partly due to their remarkable optical properties which are easily tuned by tailoring the size and shape.^{1–5} Many research groups have demonstrated how the resulting metal nanoparticles could be utilized for bionanotechnology, optoelectronic, and catalytic devices.^{6–12} Among many applications of metal nanoparticles, the interparticle electromagnetic (EM) coupling has been postulated and observed to lead to a strong enhancement of Raman scattering of adsorbed molecules.^{13–19} Surface enhanced Raman scattering (SERS) was discovered in 1977 and has been studied extensively.^{20–22} The SERS technique allows one to obtain a spectrum over a wide frequency region and shows enormous enhancement ($>10^6$ -fold) when adsorbates are on properly prepared substrates typically consisting of coinage metals, Cu, Ag, and Au. It is now widely understood that these enhancements originate from local EM field enhancement at the interstices among nanostructures.²³ For example, Pendry et al. theoretically demonstrated using Maxwell equations that the touching metallic objects could create a large EM field through the strong EM coupling as the interparticle distance decreases.²⁴ The group claimed that the collective EM effects could explain enhancements of $\sim 10^6$ in the Raman signal and their dependence on photon frequency. El-Sayed et al. performed electrodynamic simulations for nanoparticles based on the discrete dipole approximation (DDA) method and proved that there is indeed a strong EM coupling when the interparticle distance was smaller than a certain size.²⁵ Experimentally,

Moskovits et al. reported that producing a proper distance between Ag nanowires and placing an analyte within close contact between the nanowires could lead to the intense SERS enhancement.²⁶ They specifically noticed that the accessibility of analyte to the hot clefts is one of the key features in significant SERS enhancement. Murphy et al. reported that the large local EM field at the interface between a flat surface and a specifically shaped nanoparticle is the major contributor for huge SERS enhancement.²⁷ They also suggested that nanosized cubes, blocks, and dogbones generated greater SERS enhancement than spheres.

In the context of exploiting the SERS effect of metal nanoparticles, the critical features were not only used to control the physical dimensions of each particle but also ordering them into a 2- or 3-dimensional hierarchical structure in a tunable fashion.^{28–30} In our previous report, it was shown that the water/hexane interface could be used for assembling nanoparticles into 2-dimensional arrays.^{31–33} Under the given experimental conditions, the rod-like nanoparticles exhibited 1 order of magnitude higher SERS effect compared to the spherical nanoparticles.³¹ The origin of this enhancement difference was attributed to the difference of junction points within the nanoparticle films. The nanorod (NR) films have line contacts with each other, however the nanosphere (NS) films have point contacts. Of interest is the comparison of the SERS effect of such films as a function of nanorod physical dimensions. Herein, methods for synthesizing gold nanorods in different sizes, ordering them into a 2-dimensional array at water/hexane interface, stacking 2-dimensional films in a z -direction with horizontal lifting, and characterizing their corresponding SERS enhancement as a function of film thickness are described. We also carried out theoretical calculations in order to explain the observed SERS enhancement variation for each nanoparticle film. The results suggest that the interlayer coupling plays a unique role in terms of enhancing SERS effect of 3-dimensional nanoparticle films as compared with 2-dimensional nanoparticle films.

* Corresponding authors. E-mail: skkim@skku.edu (S.K.K.); spark72@skku.edu (S.P.).

[†] Department of Chemistry.

^{||} Hyosung Corporation.

[‡] Department of Energy Science.

[§] Advanced Institute of Nanotechnology.

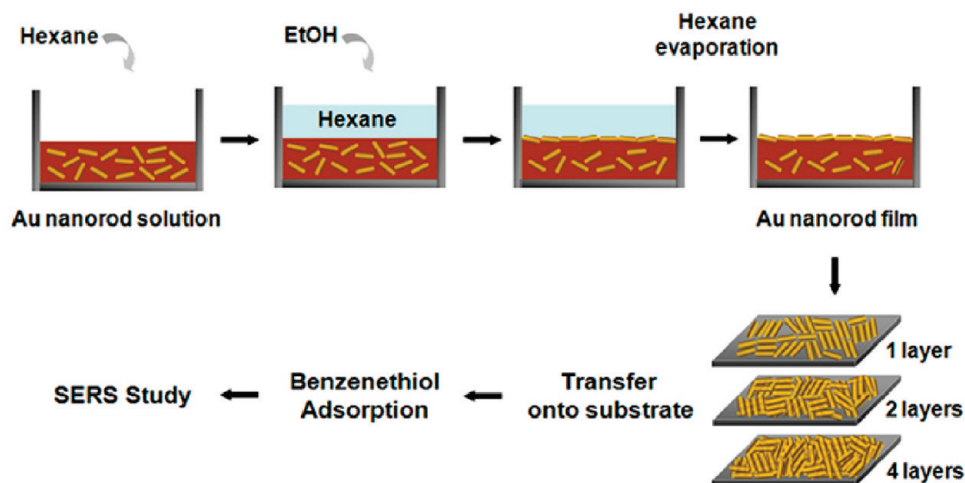


Figure 1. Schematic representation of the gold NR film formation at the water/hexane interface.

Experimental Section

$\text{HAuCl}_4 \cdot \text{H}_2\text{O}$ was purchased from KOJIMA, sodium citrate (99%) was purchased from YAKURI, sodium borohydride (98%) was purchased from JUNSEI, L(+)-ascorbic acid was purchased from KANTO chemicals, silver nitrate (99.8%) was purchased from INUIISHO chemicals, and HNO_3 (60%) was purchased from SAMCHUN. Deionized water was prepared by a Milli-Q water purification system. All glassware and Teflon-coated magnetic stir bars were cleaned with aqua regia (a volumetric ratio of 1:3 = nitric acid:hydrochloric acid, *caution!* highly oxidative and toxic), followed by copious rinsing with distilled water before drying in an oven. Field-emission scanning electron microscopy (FESEM) and transmission electron microscopy (TEM) images were obtained using a JEOL 7000F and JEOL JEM-3011, respectively. A micro-Raman spectrometer (Renishaw, InVia) was used to record the SERS. A He–Ne laser at 632.8 nm was used as the excitation laser. The excitation light of less than 0.5 mW was focused onto a sample area of approximately $1 \mu\text{m}^2$. The scattered light was collected, filtered, and dispersed in a monochromator before being detected by a cooled CCD. Each Raman spectrum was obtained with a 10 s exposure to the detector. 0.1 M of benzenethiol in ethanol was used as the analyte for the SERS measurement.

Seed Solution Preparation. Ten mL of 0.1 M CTAB was mixed with 0.125 mL of 0.02 M $\text{HAuCl}_4 \cdot 3\text{H}_2\text{O}$. 600 μL of ice-cold NaBH_4 was then added, which resulted in a color change to brownish yellow. Two different concentrations of NaBH_4 solution were used; 6 and 10 mM. Seeds prepared from 6 mM NaBH_4 were labeled as seed 1, and seeds from 10 mM NaBH_4 were seed 2.

Preparation of NRs with an Aspect Ratio ~ 2.0 ($d \approx 33$ (± 3 nm), $L \approx 67$ (± 6 nm)); Sample 1. A mixture of 2.5 mL of 20 mM $\text{HAuCl}_4 \cdot 3\text{H}_2\text{O}$, 550 μL of 0.1 M ascorbic acid, and 400 μL of 0.01 M AgNO_3 was added to 95 mL of 0.1 M CTAB solution. 120 μL of the seed 1 solution was added to the prepared growth solution and incubated for 5 h at room temperature without agitation.

Preparation of NRs with an Aspect Ratio ~ 2.2 ($d \approx 24$ (± 2 nm), $L \approx 54$ (± 3 nm)); Sample 2. A mixture of 2.5 mL of 20 mM $\text{HAuCl}_4 \cdot 3\text{H}_2\text{O}$, 550 μL of 0.1 M ascorbic acid, and 600 μL of 0.01 M AgNO_3 was added to 95 mL of 0.1 M CTAB solution. 120 μL of the seed 1 solution was added to the prepared growth solution.

Preparation of NRs with an Aspect Ratio ~ 3.1 ($d \approx 18$ (± 2 nm), $L \approx 55$ (± 5 nm)); Sample 3. A mixture of 2.5 mL of 20 mM $\text{HAuCl}_4 \cdot 3\text{H}_2\text{O}$, 550 μL of 0.1 M ascorbic acid, and 600 μL of 0.01 M AgNO_3 was added to 95 mL of 0.1 M CTAB solution. 120 μL of seed 2 solution was added to the prepared growth solution.

Preparation of NRs with an Aspect Ratio ~ 16.6 ($d \approx 18$ (± 2 nm), $L \approx 298$ (± 41 nm)); Sample 4. Two 100 mL volumetric flasks and one 1000 mL volumetric flasks labeled A, B, and C, respectively, were prepared. In flasks A and B, 45 mL of 0.1 M CTAB was mixed with 0.56 mL of 0.02 M $\text{HAuCl}_4 \cdot 3\text{H}_2\text{O}$ and 0.25 mL of 0.1 M ascorbic acid. In flask C, 450 mL of 0.1 M CTAB was mixed with 5.6 mL of 0.02 M $\text{HAuCl}_4 \cdot 3\text{H}_2\text{O}$, 2.5 mL of 0.1 M ascorbic acid, and 3 mL of 0.1 M HNO_3 . To initiate rod growth, 4 mL of the seed 2 solution was added to the solution in the flask A. 4 mL of the solution in Flask A was then transferred to flask B, and 40 mL of the solution in flask B was successively transferred to flask C. Each process was performed within 5 s with mild stirring. The resulting flask C was left undisturbed at room temperature for 12 h, and the purplish supernatant was carefully removed. A total volume of 40 mL of deionized water was added to redisperse the precipitate, and the final color of the NR solution was brown.

Results and Discussion

Figure 1 shows a schematic diagram of the formation of the 2-dimensional array of NR films at a water/hexane interface. The detailed mechanism can be found in previously reported publications and will not be described in detail.³¹ Briefly, 8 mL of gold NR aqueous solution was transferred to a Teflon cell (inner dimension, $3.0 \times 4.0 \times 1.8 \text{ cm}^3$), and 7 mL of hexane was added to form an immiscible water/hexane interface. 6 mL of ethanol was added dropwise to the surface of the water/hexane layers (0.6 mL/min, using a mechanical syringe pump), leading to trapping of the nanoparticles at the interface. Upon addition of ethanol, the surface charge of the NRs gradually decreases as the ability of water to separate charged nanoparticles diminishes by the decrease of the dielectric constant of water. The unstable NRs move to the high energy interface in order to decrease the interfacial energy between water and hexane. The key feature for the entrapment of NRs at the interface is related to how one can induce the destabilization of NRs. The prepared NRs were stabilized by a high concentration of (0.1 M) CTAB cationic surfactant. The reduction of the total

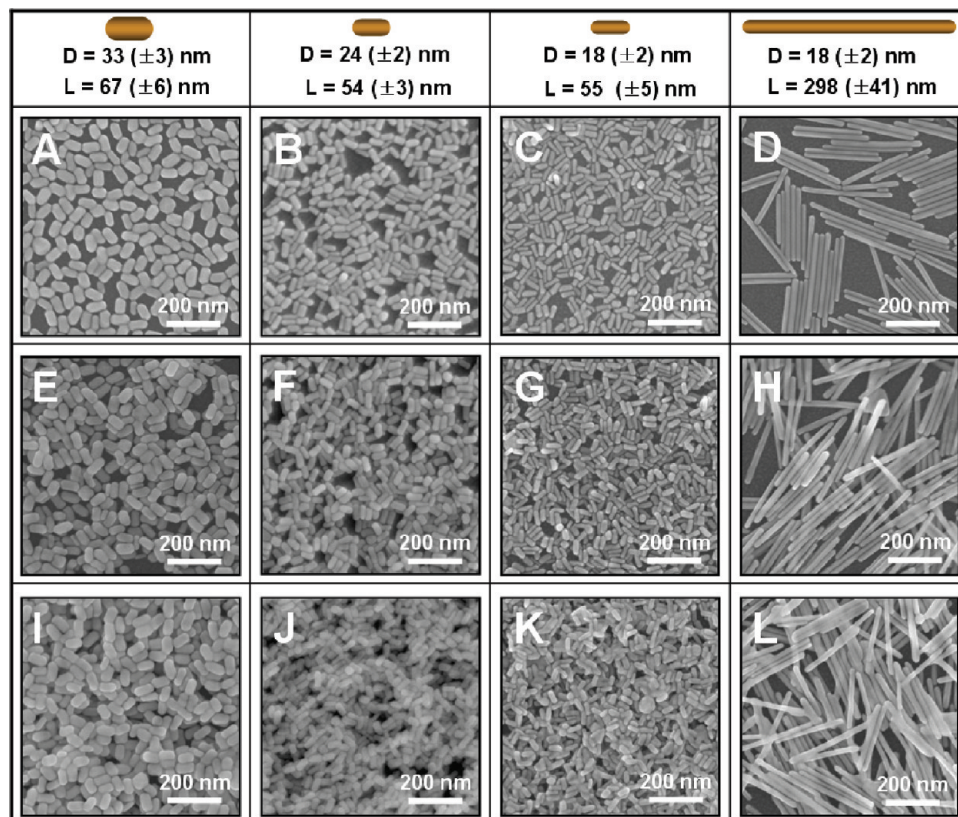


Figure 2. FESEM images for gold NR films as a function of monolayers. (A–D) for one monolayer NR for each sample. (E–H) for two monolayers. (I–L) for four monolayers.

concentration (down to approximately 0.1 mM) of CTAB by rinsing and centrifugation is very important for facile NR entrapment. When the metallic reflection becomes distinct at the interface, the hexane layer evaporates spontaneously leaving the NR films on the water surface. The resulting NR films can be transferred to other substrates. Representative FESEM images are shown in Figure 2 for a variety of NRs with different physical dimensions. Four different kinds of nanorods with different sizes and aspect-ratios were synthesized. Regardless of the physical dimensions of each NR sample, the aforementioned NR transfer process allowed one to obtain the desired NR films. As represented in the first row of Figure 2, close-packed NR films with a small fraction of voids were observed. NRs represented in Figure 2A and B have a similar aspect-ratio (2.0 and 2.2), however their absolute sizes are different. NRs shown in Figure 2B and C have a similar length (ca. 54 nm), however their aspect-ratio (2.2 and 3.1, respectively) is different due to the difference in diameters. NRs in Figure 2C and D have a similar diameter (ca. 18 nm), but the NRs in Figure 2D had an extremely long length, resulting in an aspect ratio of ca. 16.6. As demonstrated in Figure 2, the thickness of NR films was systematically tuned by the number of transfers. The second and third rows represent two and four monolayer samples of each NR, respectively. The multilayer NR films showed a morphology similar to the monolayer film, without significant aggregation.

The representative UV–vis extinction spectra of four NR samples in aqueous medium show two distinct absorption bands centered at ca. 510 nm for the transverse mode and at longer wavelength for the longitudinal mode. The latter mode shifted consistently to longer wavelengths as the NR length is increased (Figure 3). The peak position of the longitudinal surface plasmon bands significantly depends on the aspect-ratio, while the

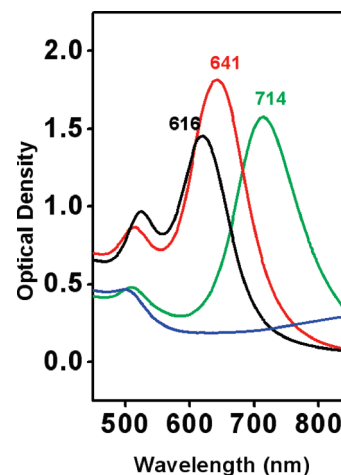


Figure 3. UV–vis extinction spectra of gold NR in water phase. Sample 1 (black trace), sample 2 (red trace), sample 3 (green trace), and sample 4 (blue trace) show different longitudinal peak positions that are indicated with numbers.

transverse mode shifts by a small degree. The longest NRs (corresponding to NRs in Figure 2D) shows only a transverse mode in the given spectrum window because the longitudinal mode shifted into the near-IR region. The absorption bands were fairly narrow, representing the monodispersity of NRs, which is consistent with the observation from the FESEM images. However, the spectrum of NR films on glass substrates exhibited different UV–vis extinction profiles. Figure 4 shows the UV–vis extinction spectra of the NRs on a glass substrate as a function of the film thickness for each NR sample. A noticeable feature was the development of broad bands in a longer wavelength region.

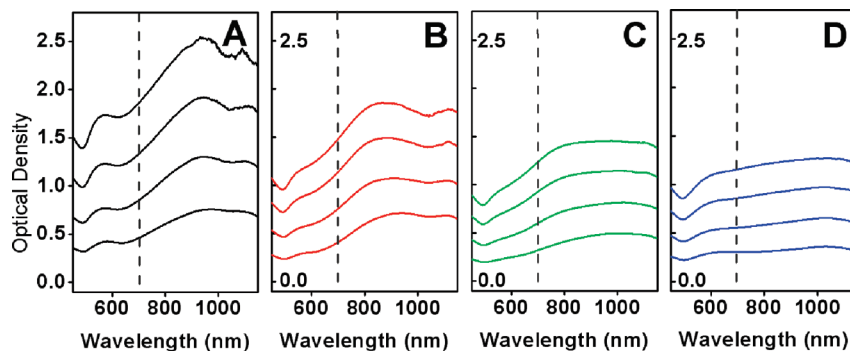


Figure 4. Extinction spectra of gold NR films with different number of monolayers (from bottom to top, one, two, three, and four monolayers). Each panel was obtained from (A) sample 1, (B) sample 2, (C) sample 3, and (D) sample 4. The dashed line represents 632.8 nm, excitation wavelength of laser for SERS measurement.

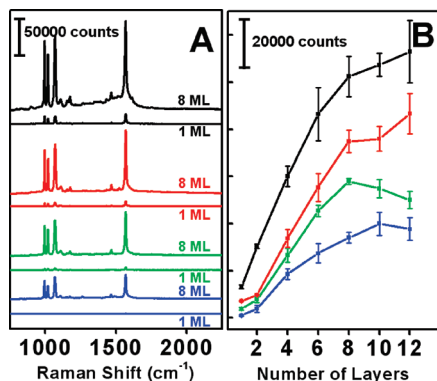


Figure 5. (A) SERS spectra of adsorbed benzenethiol on a different number of gold NRs monolayers (ML). (B) A graph for SERS intensity of a band at 1572 cm^{-1} vs different number of NR monolayer films.

The strong surface plasmon coupling among closely neighboring nanoparticles could cause the band shift and broadening.³⁴ The high surface NR coverage in the given 2-dimensional geometry induces a high-degree of surface plasmon coupling, which will eventually lead to the similar optical properties of flat metal surfaces as the surface coverage reaches 100%. As exemplified in the FESEM images (Figure 2), the resulting NRs are expected to exhibit heavy optical coupling among NRs originating from tip-to-tip, side-to-side, and tip-to-side interactions.

Another noticeable feature is the gradual increase in optical density without significant peak shifts as the NR film layer thickness increases. The high surface coverage of NRs for each layer prevents the additional positioning of NRs in voids of the predeposited NR films due to the insufficient void areas minimizing the additional EM coupling. The optical density of NR films revealed greater dependence on the diameter than the length variation because the film thickness is directly proportional to the diameter of NRs. As shown in Figure 4A–D, the optical density decreases over the investigated wavelength window as the diameter decreased.

The important feature of this report is related to the comparison of the SERS spectra obtained as a function of the number of NR monolayers. A systematic comparison of SERS enhancement based on the NR size, aspect-ratio and corresponding film thickness was obtained using adsorbed benzenethiol as a model system. In order to optimize the SERS enhancement of NR films, the aforementioned NR films constructed from four different NR samples were tested. Figure 5A shows representative SERS spectra of benzenethiol adsorbed on a single monolayer and eight monolayers of each NR film. The eight-monolayer NR films showed higher SERS enhancement compared to the single-monolayer NR films for all

samples. A comprehensive peak assignment of the spectral features has been reported elsewhere and will not be described in this report^{32,35,36} as the aim of this study was to compare the relative SERS enhancement on various NR films. It was already demonstrated that aggregates of nanoparticles induce strong SERS enhancement due to the large EM fields at the junctions of the nanoparticles. It was expected that the thicker NR films have more such junctions, and therefore higher SERS enhancement would be observed. Figure 5B shows the systematic comparison in the SERS enhancement dependence on the thickness of the four different NR samples. The SERS intensity of the adsorbate on the NR multilayer films increased up to a certain film thickness, ca. 8 monolayers. Each measurement was repeated at least three times at different spots on an individual sample. The standard deviation for each measurement was within 10%, representing fairly reproducible signals. The good reproducibility originates from the homogeneous morphology of the films as illustrated in the FESEM images. As described in a previous report, the linear increase in SERS enhancement to a certain point pertains to a simple relationship representing the enhancement factor per NR layer, $I = A \cdot n$, in which I is the SERS peak intensity, n is the number of layers, and A is the slope. Obtaining A enables a qualitative comparison of NR films with different physical dimensions under identical experimental conditions.³¹ The strongest SERS enhancement was obtained from Sample 1 (black traces). The dashed traces in the UV–vis spectra of Figure 4 indicate the excitation laser wavelength, 632.8 nm. As shown with Sample 1, the largest diameter had the largest optical density at the excitation wavelength. This suggests that SERS enhancement is dependent on resonance with the incident radiation, which is well explained by EM coupling among NRs. However, in a previous report, Murphy group reported that the nanoparticle shape was less dependent on resonance with the incident radiation source than other chemical effects.²⁷ This observation is in direct contrast to the current results. The discrepancy might originate from the different nanoparticle morphology between samples. The SERS enhancement factors in the previously report was obtained from the sandwich structure of adsorbed molecules between the flat surface and different nanoparticle shape.²⁷ However, in the current system, the signals originate mainly from the junctions and clefts among NRs. Therefore, the absolute optical density of NRs was important for maximizing the EM coupling when the excitation wavelength was in resonance with the absorbed incident light. If this was correct, then the second intensive SERS enhancement would be observed from Sample 2 based on the UV–vis extinction in Figure 2. As expected, SERS enhancement from Sample 2 (red traces) was observed in Figure

TABLE 1: Structures of Gold NR Tetramers and the Resultant Local Field Summation of the DDA Simulation

target no.	diameter (nm)	length ^a (nm)	cross-section (nm ²)	interface area (nm ²)	$\Sigma \mathbf{E} ^2(\text{interface}^b)$	$\Sigma \mathbf{E} ^2/\text{cross-section (nm}^{-2}\text{)}$
1	33	67	10 074	22 882	2.15×10^6	213
2	24	53	5562	13 786	3.20×10^5	57
3	18	55	4424	10 866	1.92×10^5	43
4	18	98	23 632	58 251	7.33×10^5	31

^a Including hemispherical caps. ^b The summation over free space cells next to gold surface cells.

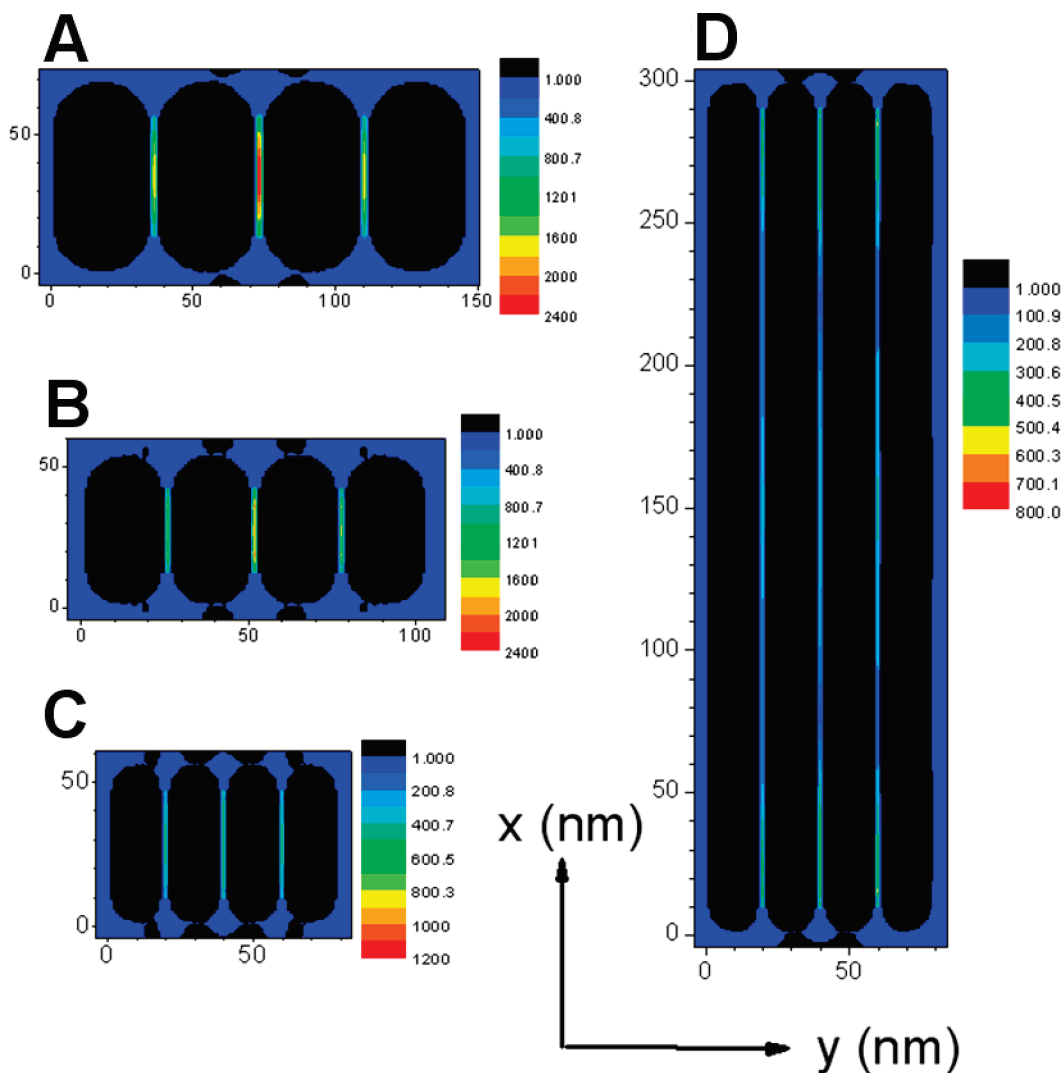


Figure 6. Maps of $|\mathbf{E}|^2$ distribution of the four rod tetramers in $z = 0$ plane. Only the calculations for y-polarized light are shown. In each target, the $|\mathbf{E}|^2$ distribution in gold area was blacked out. Notice that the color scale bars are not same for the four targets. (A–D) targets correspond to (A–D) samples shown in Figure 1.

5. This hypothesis was further confirmed from Samples 3 and 4 in which their consistent decrease in SERS enhancement matched the UV–vis optical density at the given wavelength. A theoretical consideration was used to explain the experimental observations using DDA simulations.

In the DDA method, polarizabilities of cubic grid cells that subdivide a target induced by an incident light of a fixed wavelength are solved by iteration.³⁷ The source code, DDSCAT6.1, was obtained from Professor Draine's home page.³⁸ Four different gold tetramers, whose sizes are in accord with the SERS experiments of this report, were the objects of the DDA calculation as summarized in Table 1. For the optical constants of gold, the values reported by Johnson and Christy were used.³⁹ The medium was vacuum. Each gold NR was placed in the $z = 0$ plane. The target was exposed to incident light with a wavelength of 632.8 nm, polarized along either the

x- or y-axis. The grid cells of each target had a dimension of $1 \times 1 \times 1 \text{ nm}^3$. Each NR contacted its nearest neighbors with 1 nm of free space.

A batch of induced dipole moments (\mathbf{P}) of the target grid cells was generated with a modified DDSCAT code. The local electric field (\mathbf{E}) of the induced dipole moments around the target was calculated with eq 1³⁷

$$\mathbf{E} = k^2 e^{i\mathbf{k} \cdot \mathbf{r}} \frac{\mathbf{r} \times (\mathbf{r} \times \mathbf{P})}{r^3} + e^{i\mathbf{k} \cdot \mathbf{r}} (1 - i\mathbf{k} \cdot \mathbf{r}) \frac{[r^2 \mathbf{P} - 3\mathbf{r}(\mathbf{r} \cdot \mathbf{P})]}{r^5} \quad (1)$$

where \mathbf{r} is the coordinate of free space cell around the target and \mathbf{k} is the wavevector ($r = |\mathbf{r}|$, and $k = |\mathbf{k}|$).

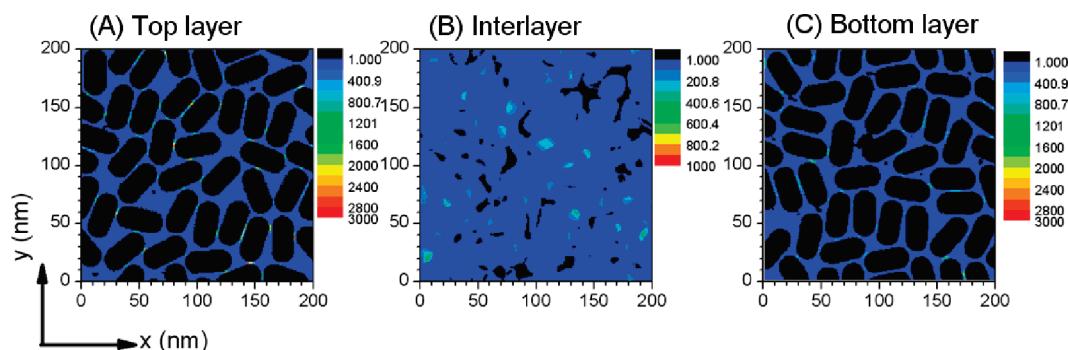


Figure 7. Maps of $|E|^2$ distribution for the random loose packing of 20 nm diameter, 41 nm length nanorods. Double layer cases for x -polarized light are shown. (A) xy cross-section of the top layer (B) xy cross-section ($z = 0$) of the interlayer (C) xy cross-section of bottom layer. Notice that color scale bar of the plot (B) is different from (A) and (C). In the plots of (A) and (C), some $|E|^2$ values are higher than the color scale bar maximum (3000). They are denoted as white colors. The maximum E^2 values are 5180 for (A) and 3720 for (B).

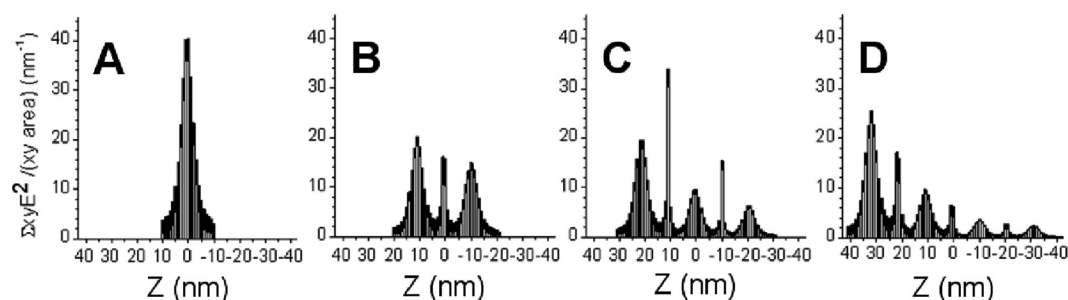


Figure 8. Sum of $|E|^2$ over xy plane along the z -axis (normal to incident light), divided by the xy area. (A) one, (B) two, (C) three, (D) four NR layers (see texts for details).

Figure 6 illustrates maps of the $|E|^2$ distribution for the four targets in the $z = 0$ plane. Only the calculations for y -polarized light (along the short axis of NR) are shown as the $|E|^2$ values because those for x -polarized light were smaller by an order of magnitude. In the four targets, a high local electric field was formed at the 1 nm contact space between two rods. The maximum intensity of the local electric field was ordered as Target 1 > 2 > 3 > 4, which is consistent with the order of SERS intensities in the experiment. Target 4 has the largest contact area, however the local field at the contact space was rather low.

Most of the large $|E|^2$ values are found at the free space cells that are neighbors of gold surface cells. We define such free space cells as the interface cells. Since the SERS effect is dominated by contributions of analyte molecules that bind strongly to metal surface, the $|E|^2$ at the interface cells of each target was summed over. The averages of $|E|^2$ for the x - and y -polarized light were taken for the final $\Sigma|E|^2$. In Table 1, the fourth column is the xy cross-section area of each target. The fifth column is the interface area, which may be proportional to the number of adsorbates in the SERS experiments. The interface area divided by the cross-section area produces 2.5 ± 0.25 for all of the targets, which implies that the number of adsorbates per given area of each target is constant within 10%. The sixth column is the sum of the local electric field intensities over the interface area. Finally, the seventh column is the sum of local electric field intensities normalized by the cross-section area, which is ordered in same way as the experimental SERS measurements.

The fact that the high local field is created by the short axis excitation on the NR in each target geometry is noteworthy. This is related to the side-by-side arrangement of NRs. In other words, the interparticle plasmon coupling in the given arrangement is most effective when the excitation polarization direction is perpendicular to the long axis of NRs.²³ In a diameter range

of tens of nm, the short axis excitation increases as the NR diameter is increased. (For example, the Mie calculation for spherical gold nanoparticles shows that the plasmon band increases with the diameters up to 50 nm.⁴¹) When NRs of an equal diameter but different lengths are compared, longer NRs have larger contact area in the side-by-side assembly but generate less intensive interparticle plasmon coupling (see Figure 6D, for example.). Therefore, the reason for the SERS enhancement for the assemblies of NR in different size and shape is explained by a different degree of plasmon coupling along the short axis of NRs.

In order to estimate the $|E|^2$ distribution of multilayer NRs, we used the finite different time domain (FDTD) method. For the FDTD calculation, we used a MEEP program (version 0.20.3) which is developed by Johnson.⁴² Along the light propagating z -axis, two 300 nm thick perfect matching layers (PML) were set at both ends.⁴² A light source was set at 30 nm below the top PML and it generated an electromagnetic field which propagated as a plane wave along the z axis. The target was placed at the middle ($z = 0$), 970 nm below the light source. A periodic boundary condition was applied to all x , y , and z axes, so that the target structure is a repeating unit of 2-dimensional film. Forty or forty-one rods of 20 nm diameter and 41 nm length (including caps) were packed randomly with a contact spacing of 1 nm in 200×200 nm². Here, rods at the x and y boundaries were arranged to satisfy the periodic boundary condition (e.g., see Figure 7). For a multilayer NR, rods in each layer were arranged independently and placed up or down by (sphere diameter + 1 nm) from the lower or upper layer. For the dispersion equation of Au optical constants, the complex dielectric constant data of Johnson and Christy were used to fit a sum of two Lorentzian functions.³⁹

Figure 7 shows examples of the $|E|^2$ distribution for NR. The cases of the double layer for x -polarized light are shown. In the top layer (Figure 7A), high local field is apparent at some contact

spacing cells between two rods. The high local field is somewhat reduced at the bottom layer (Figure 7C) as most of the incident light is absorbed at the top layer. In Figure 7B, the $|\mathbf{E}|^2$ distribution at the interlayer is shown. Rather high local field is apparent at some interlayer contact spaces.

The $|\mathbf{E}|^2$ distribution of each target was then summed over a xy cross-sectional area along the z -axis ($\sum_{xy} \mathbf{E}^2$), and divided with the xy area for normalization. Figure 8 is the result. The ordinate of Figure 8 corresponds to cellular average of $|\mathbf{E}|^2$ in the xy cross-section. In a single layer cases (Figure 8A), there is a peak at $z = 0$, where contact between two rods in 2D array is made. In the double layer case (Figure 8B), there are two broad peaks. The peak at positive z is for the top layer and the peak at negative z is for the bottom layer. Intensity of the bottom layer peak is lower than that of the top layer peak. There is also a peak at $z = 0$. This corresponds to the local field produced at the interlayer contact. This peak is sharp and large. The Plasmon coupling between layers is evident in the FDTD calculation. In other words, the induced dipoles created preferentially at the top layer by the incident light may have induced dipoles at the lower layer. The interlayer peaks of triple layers and quadruple layers show the same trend, reflecting the measure of interlayer contact in each target structure. Intensities of these broad peaks decrease as the layer goes to the bottom, as the incident light does not reach the bottom layers. In experiments, spheres or rods of an upper layer prefer to sit at interstitial sites of the lower layer. However, this condition was not satisfied in computation. Considering these limitations in packing structures, the interlayer Plasmon coupling must be more effective than our calculation shows.

Conclusion

This report demonstrates how a nanoparticle film could be systematically prepared with 2- or 3-dimensional structures. The influence of the physical dimensions of the individual building blocks on their corresponding enhancement of the SERS effect was studied through the systematic construction of 2- or 3-dimensional NR films. It should be noted that since the cooperative EM coupling at interstices among nanoparticles, often dubbed as "hot spots", is a major reason for significant SERS enhancement, there should be a general approach to forming controlled aggregates. As demonstrated in this report, the water/hexane interface allows for control of such aggregate structures. The nanoparticle films generated from different NRs illustrated that the individual nanoparticle structure was important in terms of harvesting their cooperative EM coupling for SERS application. The suggested enhancement factor per layer (A) depending on the NR size and aspect-ratio was obtained from a plot of the peak intensity versus the number of layers. The enhancement factor is a relative value and can vary depending on experimental conditions, such as the laser power, excitation wavelengths, and acquisition time. However, under given experimental conditions, the comparison of (A) factors enables the systematic evaluation of SERS enhancement. Both the experimental and theoretical simulation results showed that the strong EM coupling could be generated from large NR aggregates, and the resulting SERS enhancement correlated well with the absorbance change of NR films. In contrast to the case of 2-dimensional nanoparticle films, the FDTD calculation results suggest that the EM coupling at interlayer of 3-dimensional nanoparticle films plays a roll in enhancing the total EM field.

Acknowledgment. This work was supported by the Korea Research Foundation Grant funded by the Korean Government

(MEST, KRF-2008-005-J00702) and the Korea Science and Engineering Foundation (Nano R&D program: 2008-04285, 2008-0060482).

References and Notes

- (1) *Colloidal Gold*; Hyatt, M. A., Ed.; Academic Press: New York, 1989.
- (2) Vijaya Sarathy, K.; Raina, G.; Yadav, R. T.; Kulkarni, G. U.; Rao, C. N. R. *J. Phys. Chem. B* **1997**, *101*, 9876.
- (3) Freeman, R. G.; Graber, K. C.; Allison, K. J.; Bright, R. M.; Davis, J. A.; Guthrie, A. P.; Hommer, M. B.; Jackson, M. A.; Smith, P. C.; Walter, D. G.; Natan, M. J. *Science* **1995**, *267*, 1629.
- (4) Wang, H.; Brandl, D. W.; Nordlander, P.; Halas, N. J. *Acc. Chem. Res.* **2007**, *40*, 53.
- (5) Cao, Y. C.; Jin, R.; Mirkin, C. A. *Science* **2002**, *297*, 1536.
- (6) Park, S.; Wieckowski, A.; Weaver, M. J. *J. Am. Chem. Soc.* **2003**, *125*, 2282.
- (7) Carrette, L.; Friedrich, K. A.; Stimming, U. *ChemPhysChem* **2000**, *1*, 162.
- (8) Trindade, T. *Chem. Mater.* **2001**, *13*, 3843.
- (9) Link, S.; Wang, Z. L.; El-Sayed, M. A. *J. Phys. Chem. B* **1999**, *103*, 3529.
- (10) Freeman, R. G.; Hommer, M. B.; Grabar, K. C.; Jackson, M. A.; Natan, M. J. *J. Phys. Chem.* **1996**, *100*, 718.
- (11) Aliev, F. G.; Correa-Duarte, M. A.; Mamedov, A.; Ostrander, J. W.; Giersig, M.; Liz-Marzan, L. M.; Kotov, N. A. *Adv. Mater.* **1999**, *11*, 1006.
- (12) Cho, S.-J.; Kauzlarich, S. M.; Olamit, J.; Liu, K.; Grandjean, F.; Rebbouh, L.; Long, G. J. *J. Appl. Phys.* **2004**, *95*, 6804.
- (13) Aravind, P. K.; Nitzan, A.; Metiu, H. *Surf. Sci.* **1981**, *110*, 189.
- (14) Inoue, M.; Ohtaka, K. *J. Phys. Soc. Jpn.* **1983**, *52*, 1457.
- (15) Xu, H. X.; Kall, M. *Chem. Phys. Chem.* **2003**, *4*, 1001.
- (16) Jiang, J.; Bosnick, K.; Maillard, M.; Brus, L. *J. Phys. Chem. B* **2003**, *107*, 9964.
- (17) Murphy, C. J.; Gole, A. M.; Hunyadi, S. E.; Orendorff, C. J. *Inorg. Chem.* **2006**, *45*, 7544.
- (18) Suzuki, M.; Niidome, Y.; Kuwahara, Y.; Terasaki, N.; Inoue, K.; Yamada, S. *J. Phys. Chem. B* **2004**, *108*, 11660.
- (19) Yang, Y.; Xiong, L.; Shi, J.; Nogami, M. *Nanotechnology* **2006**, *17*, 2670.
- (20) Jeanmaire, D. L.; Van Duyne, R. P. *J. Electroanal. Chem.* **1977**, *84*, 1.
- (21) Albrecht, M. G.; Creighton, J. A. *J. Am. Chem. Soc.* **1977**, *99*, 5215.
- (22) Moskovits, M. *J. Chem. Phys.* **1978**, *69*, 4159.
- (23) *Surface-Enhanced Raman Scattering*; Kneipp, K., Moskovits, M., Kneipp, H., Ed.; Springer: Germany, 2006.
- (24) Garcia-Vidal, F. J.; Pendry, J. B. *Phys. Rev. Lett.* **1996**, *77*, 1163.
- (25) Jain, P. K.; Eustis, S.; El-Sayed, M. A. *J. Phys. Chem. B* **2006**, *110*, 18243.
- (26) Lee, S. J.; Morrill, A. R.; Moskovits, M. *J. Am. Chem. Soc.* **2006**, *128*, 2200.
- (27) Orendorff, C. J.; Gole, A.; Sau, T. K.; Murphy, C. J. *Anal. Chem.* **2005**, *77*, 3261.
- (28) Yoge, D.; Efrima, S. *J. Phys. Chem.* **1988**, *92*, 5754.
- (29) Tao, A.; Kim, F.; Hess, C.; Goldberger, J.; He, R.; Sun, Y.; Xia, Y.; Yang, P. *Nano. Lett.* **2003**, *3*, 1229.
- (30) Jeong, D. H.; Zhang, Y. X.; Moskovits, M. *J. Phys. Chem. B* **2004**, *108*, 12724.
- (31) Yun, S.; Park, Y.-K.; Kim, S. K.; Park, S. *Anal. Chem.* **2007**, *79*, 8584.
- (32) Jung, H. Y.; Park, Y.-K.; Park, S.; Kim, S. K. *Anal. Chim. Acta* **2007**, *602*, 236.
- (33) Park, Y.-K.; Park, S. *Chem. Mater.* **2008**, *20*, 2388.
- (34) Camden, J. P.; Dieringer, J. A.; Wang, Y.; Masiello, D. J.; Marks, L. D.; Schatz, G. C.; Van Duyne, R. P. *J. Am. Chem. Soc.* **2008**, *130*, 12616.
- (35) Joo, T. H.; Kim, M. S.; Kim, K. *J. Raman Spectrosc.* **1987**, *18*, 57.
- (36) Taylor, C. E.; Pemberton, J. E.; Goodman, G. G.; Schoenfish, M. H. *Appl. Spectrosc.* **1999**, *53*, 1212.
- (37) (a) Draine, B. T.; Flatau, P. J. *J. Opt. Soc. Am. A* **1994**, *11*, 1491.
- (b) Draine, B. T.; Goodman, J. J. *Astrophys. J.* **1993**, *405*, 685.
- (38) Draine, B. T.; Flatau, P. J.; The Discrete Dipole Approximation Code DDSCAT (Version 6.1), available from <http://www.astro.princeton.edu/~draine/>.
- (39) Johnson, P. B.; Christy, R. W. *Phys. Rev. B* **1972**, *6*, 4370.
- (40) Kelly, K. L.; Coronado, E.; Zhao, L. L.; Schatz, G. C. *J. Phys. Chem. B* **2003**, *107*, 668.
- (41) Doremus, R. H. *J. Chem. Phys.* **1964**, *40*, 2389.
- (42) Johnson, S. C.; MIT Electromagnetic Equation Propagation, available from <http://ab-initio.mit.edu/wiki/index.php/Meep>.